# Coupled channel description of $^{16}O + {}^{142,144,146}Nd$ scattering around the Coulomb barrier using a complex microscopic potential

Samit Mandal [a,b,1], T. Madhusoodhanan [c], Subinit Roy [d,*], S. Ray [b], H. Majumdar [d], S. Datta [e], S.S. Ghugre [f], S. Ghosh [a], A. Mandal [a], D.K. Avasthi [a], S.K. Datta [a]

[a] *Nuclear Science Centre, Post Box 10502, New Delhi 110067, India*
[b] *Department of Physics, University of Kalyani, Kalyani 741235, India*
[c] *Department of Physics, Bangalore University, Bangalore 560056, India*
[d] *Saha Institute of Nuclear Physics, Sector I, Block AF, Bidhannagar, Calcutta 700064, India*
[e] *Department of Physics, University of Calcutta, Calcutta 700009, India*
[f] *IUC–DAEF, Sector III, Block LB, Bidhannagar, Calcutta 700091, India*

## Abstract

Angular distributions of elastic scattering and inelastic scattering from $2_1^+$ state are measured for $^{16}O + {}^{142,144,146}Nd$ systems at several energies in the vicinity of the Coulomb barrier. The angular distributions are systematically analyzed in coupled channel framework. Renormalized double folded real optical and coupling potentials with DDM3Y interaction have been used in the calculation. Relevant nuclear densities needed to generate the potentials are derived from *shell model* wavefunctions. A truncated shell model calculation has been performed and the calculated energy levels are compared with the experimental ones. To simulate the absorption, a 'hybrid' approach is adopted. The contribution to the imaginary potential of couplings to the inelastic channels, other than the $2_1^+$ target excitation channel, is calculated in the Feshbach formalism. This calculated imaginary potential along with a short ranged volume Woods–Saxon potential to simulate the absorption in fusion channel reproduces the angular distributions for $^{16}O + {}^{146}Nd$ quite well. But for $^{16}O + {}^{142,144}Nd$ systems additional surface absorption is found to be necessary to fit the angular distribution data. The variations of this additional absorption term with incident energy and the mass of the target are explored.

* Corresponding author.
  *E-mail address:* subinit@hp1.saha.ernet.in (S. Roy).
[1] Present address: GSI, Darmstadt, Germany.

## 1. Introduction

In quasi elastic scattering of heavy ions at energies near the Coulomb barrier, the relative motion of the interacting nuclei are known to be dominated by strong coupling between the individual reaction channels [1–6]. These couplings, on the one hand, dynamically polarize the real potential inducing a marked energy dependence of its strength around the Coulomb barrier energies and, on the other hand, contribute significantly to the absorptive potential for elastic scattering at large distances. The extraordinary energy dependence of the real potential, the so-called *threshold anomaly*, was experimentally observed [7–10] and was demonstrated to be dispersively connected with an increase with the energy of the imaginary potential accounting for the increasing number of open reaction channels absorbing the incident flux [11,12].

The threshold behaviour has been shown to occur in many heavy ion scattering systems [13]. In recent years, several attempts have been made to understand the polarization effect and its dependence on the structure of the colliding nuclei by evaluating the nucleus–nucleus potential on a microscopic basis using the formalism proposed by Feshbach [14–19]. In a microscopic approach to the optical potential, the real part is derived by folding an effective nucleon–nucleon interaction with the densities of the colliding nuclei. The folding model, incorporating the structure informations directly in the evaluation of the real potential, is widely and successfully used for describing the heavy ion elastic scattering [20–23]. To derive the imaginary component microscopically several methods have been adopted [1,24–27]. Of these the model proposed by Vinh Mau et al. [27] calculates the total Feshbach potential considering all possible closed and open channels through the closure approximation. A fairly good agreement was observed between the calculation and the experiment for systems like $^{16}$O + $^{208}$Pb, $^{32}$S + $^{40}$Ca and $^{35,37}$Cl + $^{24}$Mg [16,28–32]. The model has been further modified by Pacheco et al. [16], for the conditions where a reduced number of channels control the absorption. When the energy of the collision is close to the Coulomb barrier and the colliding systems are deformed, it has been demonstrated that it is necessary to calculate the polarization potential contribution separately for each of the dominant nonelastic channel. In a detailed investigation on a number of different systems, both deformed and spherical, it was observed that the microscopic imaginary potential having contributions from the dominant inelastic excitations only is sufficient to reproduce the total absorption in strongly deformed systems [17]. Whereas for spherical and weakly deformed systems the corresponding absorption, localized in a narrow surface region, is weak and necessitates the introduction of a long range absorptive term representing the absorption in transfer channels. However, elastic scattering is unlikely to be very sensitive to the absorptive potential near the barrier. On the other hand, inelastic scattering or transfer reactions where the wavefunction plays an important role, will be more sensitive to the

details of the potential. Hence, a simultaneous description of elastic and inelastic angular distributions will be of further interest.

In our present study, we made an attempt to describe the elastic and first $2^+$ inelastic angular distributions for $^{16}O + {}^{142,144,146}Nd$ systems measured around the Coulomb barrier energies using the microscopically derived potentials, both real and imaginary, in a coupled channel (CC) framework. The measurements have been performed at incident enegies of 65, 70, 74 and 78 MeV, i.e., from the top of the barrier to about 12 MeV above. In the CC calculation, the renormalized folded M3Y potential has been used as the real potential and the imaginary component is derived from contributions from different target and projectile excitations following Pacheco et al. [16,17]. Since explicit coupling to the first $2^+$ state is considered, the microscopically calculated imaginary component will not contain the contribution from this excitation channel. In these Nd isotopes, the nucleus $^{144}Nd$ represents an intermediate step in the *shape transition* from spherical $^{142}Nd$ with $N = 82$ neutron shell closed to the transitional–vibrational nucleus $^{146}Nd$ [33]. These nuclei with large transitional $B(E2)$ values are quite soft towards quadrupole excitations. Hence, the excitation to the first $2^+$ state will be one of the major contributors in the derivation of imaginary potential. Thus the CC analysis with an imaginary potential not containing the contribution of the dominant $2^+$ excitation will provide a suitable basis to explore the effect of other couplings in the absorption process. This is especially true at near barrier energies where only a few of the reaction channels contribute in producing the absorption.

The other important aspect of this study is the determination of the coupling potential corresponding to $0^+ \rightarrow 2^+$ transition in the CC analysis using the folding model approach. The necessary transition density is derived from *shell model* wavefunctions. A truncated shell model calculation has been performed to obtain the occupation probabilities and the one body density matrices (OBDM) for constructing the densities. In recent years several shell model calculations have been carried out for $^{142}Nd$ nucleus as a member of the $N = 82$ isotones [34–37]. However, to the best of our knowledge, no such calculations have been reported for $^{144}Nd$ and $^{146}Nd$ isotopes with two- and four-valence neutrons over the $N = 82$ closed shell. A section with the details of the calculation has been included and a comparison of the calculated energy levels with the experimental energy values has been shown.

The paper has been organized as follows. The introduction will be followed by a description of the experiment in Section 2. The details of the derivation of the densities, the potentials and the analysis of the data with the derived potentials will be provided in Section 3. Finally, we will discuss and summarise our observations in the last section.

## 2. Experimental set-up

The experiment was carried out using the 15UD Pelletron Accelerator at Nuclear Science Centre (NSC), New Delhi. $^{16}O$ beam was produced in a SNICS ion source, accelerated (in the energy range 65–78 MeV), momentum analysed and allowed to impinge on Nd targets. Beam current was maintained between 5 to 40 pnA. The neodymium targets were made by vacuum evaporation of enriched $^{142,144,146}Nd$ oxide sandwiched between

Table 1
Thicknesses of different isotopically enriched targets

| ISOTOPE | Enrichment % | Thickness of carbon backing µg/cm$^2$ | Thickness of neodymium oxide µg/cm$^2$ | Thickness of coating carbon layer µg/cm$^2$ |
|---|---|---|---|---|
| $^{142}$Nd$_2$O$_3$ | 98.26 | 17.7 | 57.6 | 3.0 |
| $^{144}$Nd$_2$O$_3$ | 97.51 | 10.0 | 45.0 | 3.0 |
| $^{146}$Nd$_2$O$_3$ | 97.63 | 6.0 | 45.0 | 2.5 |

two carbon foils [38]. Thickness and the enrichment of the neodymium targets are given in the Table 1.

The angular distribution of the elastic and inelastic scattering was measured in a General Purpose Scattering Chamber (GPSC) [39] of diameter 1.5 m. Ten silicon surface barrier (SB) and passivated ion implanted planner surface (PIPS) detectors of 300 µm depletion depth were used and arranged in two movable arms on both sides of the beam axis. The average effective solid angle subtended by each silicon detector was between 3.5 msr to 7.5 msr. Two monitor detectors (300 µm) were placed symmetrically at $9.8° \pm 1°$ on either side of the beam. The monitors subtended an angle of $0.2°$ at the target. An entrance collimator of 2 mm diameter was used at a distance of 10 cm from the target. The beam was properly steered to keep the elastic peak count in the two monitor detectors identical within 5%. Standard electronics were used, and the list mode data was recorded in a Micro-VAX computer using the data acquisition programme ONLINE.

The incident energies chosen were 65, 70, 74 MeV for $^{16}$O on $^{142}$Nd and 65, 70, 74, 78 MeV for $^{16}$O on $^{144,146}$Nd. The angular distributions were measured at angles in the region from $30°$ to $164°$ (in lab.) in steps of $2°$ to $6°$. A few overlapping angles were used for different detectors to check the consistency of the data. The results of such measurements (properly normalised for solid angle) agree within statistics. Typical spectra are shown in Figs. 1 and 2. In the spectra, peaks marked as 'Ta' are due to the contamination from tantalum crucible used for vacuum evaporation of neodymium targets. However, the Ta peaks were kinematically well separated from the elastic peaks of the Nd isotopes at all the measured angles. The overall resolution obtained in different detectors varied from 250–450 keV.

The absolute cross section values were obtained by normalising the yield to the monitor counts under the elastic peak. The cross section at the monitor angle is well described by Rutherford cross section. The absolute error is estimated to be less then 10% for elastic and 20% for inelastic data. The relative error is found to be less than 5%.

## 3. Analysis

The model potential used in the coupled channel (CC) analysis has the form

$$U(E, \mathbf{R}) = \left[ V_0(E, \mathbf{R}) + \Delta V_{\mathrm{R}} \right] + i W(E, \mathbf{R}) + V_{\mathrm{C}}. \tag{1}$$

$V_0(E, \mathbf{R})$ is the average interaction between the two nuclei in the absence of any excitation and includes the exchange terms that arise from antisymmetrisation between the two
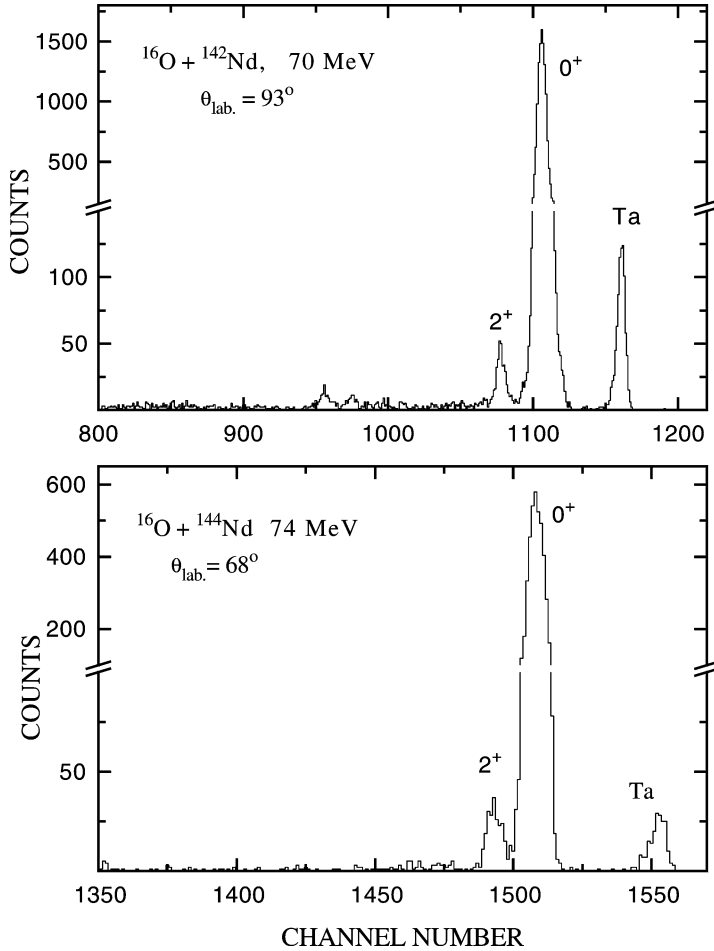
Fig. 1. Energy spectrum of particles from the elastic and inelastic scattering of $^{16}$O on $^{142}$Nd at $E_{lab} = 70$ MeV and $\theta_{lab} = 93°$ (top) and scattering of $^{16}$O on $^{144}$Nd at $E_{lab} = 74$ MeV and $\theta_{lab} = 68°$ (bottom). The peaks marked Ta are from tantalum contamination.

ions resulting in weak energy dependence of $V_0$. The real polarization part $\Delta V_R(E, \mathbf{R})$ originates from the coupling of elastic channel to other nonelastic channels and it has the contributions from both the *open* and *closed* reaction channels. The imaginary part $W(E, \mathbf{R})$, to start with, is composed of two components

$$W(\mathbf{R}, E) = W_F(\mathbf{R}) + W_{fes}(\mathbf{R}, E), \tag{2}$$

where $W_{fes}(\mathbf{R}, E)$ is the imaginary polarization potential and it depends on the number of open reaction channels. Details of the calculation of this microscopic imaginary potential is given in a following section. $W_F(\mathbf{R})$ has a squared volume Woods–Saxon form and is chosen to simulate the ingoing wave boundary condition for fusion. This interior imaginary potential has the parameters of $W_0 = 60$ MeV, $r_F = 1.0$ fm and $a_F = 0.4$ fm. This potential
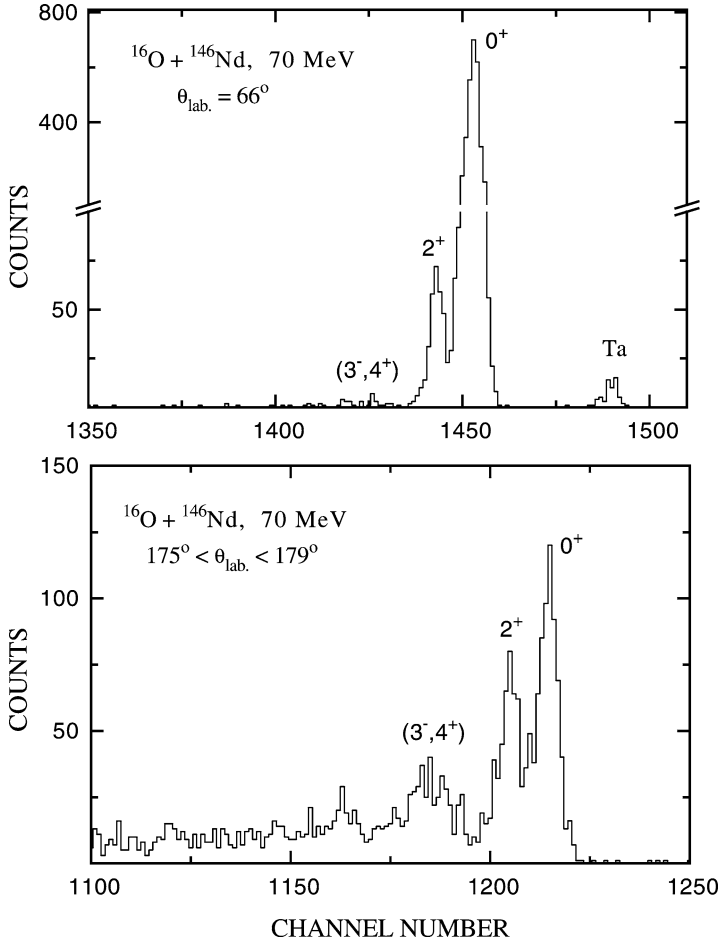
Fig. 2. Energy spectrum of particles from the elastic and inelastic scattering of $^{16}O$ on $^{146}Nd$ at $E_{lab} = 70$ MeV and $\theta_{lab} = 66°$ (top). The peak marked Ta is from tantalum contamination. The angular detector spectrum at an extreme backward angle is shown in the figure below.

has not been varied with incident energy. The same $W_F$ is used for all the three isotopes. $V_C$ in (1) denotes the Coulomb potential.

## 3.1. Folded potentials

The real parts of optical potential and the transition potential are calculated by folding an effective two-body interaction with the relevant densities of the two interacting nuclei. The energy-dependent direct and exchange components of the potential are expressed as [20,22],

$$V_D(E, \mathbf{R}) = \int \rho_1(\mathbf{r}_1)\rho_2(\mathbf{r}_2)v_D^{nn}(\rho, E, r)\, d^3r_1\, d^3r_2, \tag{3}$$

$$V_{\text{EX}}(E, \mathbf{R}) = \int \rho_1(\mathbf{r}_1, \mathbf{r}_1 + \mathbf{r}) \rho_2(\mathbf{r}_2, \mathbf{r}_2 - \mathbf{r}) v_{\text{EX}}^{\text{nn}}(\rho, E, r) e^{\frac{i\mathbf{k}(\mathbf{R})\mathbf{r}_{12}}{M}} d^3 r_1 \, d^3 r_2 \qquad (4)$$

where $\rho_i(\mathbf{r}_i), i = 1, 2$, denote the densities of respective nuclei and $v_{\text{D/EX}}^{\text{nn}}(\rho, E, r)$ is the energy- and density-dependent direct/exchange component of the effective nucleon–nucleon interaction. The coordinate $\mathbf{r}_{12}$ is equal to $\mathbf{r}_2 - \mathbf{r}_1 + \mathbf{R}$, where $\mathbf{R}$ is the centre to centre separation between the two interacting nuclei. $\mathbf{k}(\mathbf{R})$, the relative motion momentum, is expressed as

$$k^2(\mathbf{R}) = \frac{2mM}{\hbar^2} \big[ E_{\text{cm}} - V(E, \mathbf{R}) - V_{\text{C}}(\mathbf{R}) \big], \qquad (5)$$

with $M$ the reduced mass, $m$ the nucleon mass in MeV, $E_{\text{cm}}$ the centre-of-mass energy and $E$ the incident energy in laboratory. $V_{\text{C}}(\mathbf{R})$ is the Coulomb potential and $V(E, \mathbf{R})$ denotes the direct component of the folded potential.

The direct and the exchange components have been derived using the folding formulae in momentum space as detailed in Ref. [20]. In the derivation of the exchange potential $V_{\text{EX}}(E, \mathbf{R})$, however, we have chosen a closed expression for the potential in terms of a series expansion of the Bessel functions [21]. The approximation yields equivalent result as obtained in the iterative procedure, especially for the energy domain chosen by us where the scattering is more sensitive to the potential at large radius.

### 3.1.1. The interaction

The semi-realistic M3Y interaction [40] is chosen as the effective nucleon–nucleon interaction $v^{\text{nn}}$ in the present analysis. The interaction has been applied to heavy-ion scattering at energies above of 5 MeV/nucleon with reasonable success [20–22]. The direct part of the interaction is given as

$$v_{\text{D}}^{\text{nn}}(r) = 7999.0 \frac{e^{-4r}}{4r} + 2134.25 \frac{e^{-2.5r}}{2.5r}. \qquad (6)$$

A finite-range interaction term [20]

$$v_{\text{EX}}^{\text{nn}}(r) = 4631.8 \frac{e^{-4r}}{4r} + 1787.13 \frac{e^{-2.5r}}{2.5r} + 7.8474 \frac{e^{-0.7027r}}{0.7027r} \qquad (7)$$

has been adopted to calculate the exchange contribution in the potential. The effect of density dependence, though not so prominent for extremely peripheral collisions, is included as an exponentially varying multiplicative factor

$$F(\rho) = c \big[ 1 + \alpha e^{-\beta\rho} \big] \qquad (8)$$

with $c = 0.2845$, $\alpha = 3.6391$ and $\beta = 2.9605$ fm$^3$ [20,41]. The density $\rho$ in the expression is the sum of densities of the colliding nuclei at midpoint of the internucleon distance. Finally, the interaction is made to depend explicitly on energy through an additional product term $g(E) = (1 - 0.002E)$ [20,41].

### 3.1.2. Shell model calculations for nuclear densities

Nuclear ground-state and transition densities are determined from the shell model wavefunctions. The code OXBASH [42] has been used to generate the wavefunctions.

We have defined the *model space*, in the shell model calculation, to consist of spherical single particle orbitals from $N = 4$ oscillator shell $(1d_{5/2}, 0g_{7/2}, 1d_{3/2}, 2s_{1/2})$ plus the intruder $0h_{11/2}$ orbital from $N = 5$ oscillator shell for 10 valence protons of Nd isotopes over $Z = 50$ closed shell and orbitals from $N = 5$ oscillator shell $(0h_{9/2}, 1f_{7/2}, 1f_{5/2}, 2p_{3/2}, 2p_{1/2})$ plus the intruder orbital $0i_{13/2}$ from $N = 6$ shell for the valence neutrons of $^{144,146}$Nd isotopes over $N = 82$ closed neutron shell. The $^{132}$Sn ($Z = 50, N = 82$) is taken to be the core. The *model space* is coded as *Z50N82* in OXBASH.

However, a full scale shell model calculation with a large basis being not feasible with our available computational ability, we have followed a *truncation scheme*, as described in Ref. [43], in the present analysis. A partition **P** that specifies a set of occupancies for the orbits under consideration is defined. The proton and neutron orbitals outside the $^{132}$Sn ($Z = 50, N = 82$) core are included in this partition **P** as:

$$\mathbf{P} = \left[ \pi \left\{ (\mathbf{s}_{1/2})^{p1}, (\mathbf{d}_{5/2})^{p2}, (\mathbf{d}_{3/2})^{p3}, (\mathbf{g}_{7/2})^{p4}, (\mathbf{h}_{11/2})^{p5} \right\} \right.$$
$$\left. \times \nu \left\{ (h_{9/2})^{n1}, (f_{7/2})^{n2}, (f_{5/2})^{n3}, (p_{3/2})^{n4}, (p_{1/2})^{n5}, (i_{13/2})^{n6} \right\} \right], \tag{9}$$

where $p(i)$ and $n(i)$ are the numbers of protons and neutrons respectively, occupying the orbitals. Table 2 shows the restrictions imposed for different **P** partitions in the shell model calculation. One advantage of this procedure is that, since only the most dominant partitions are considered for a particular state, the renormalization of the *two-body interaction* to incorporate the effects of the neglected partitions need not be large.

The *effective interaction* used in the shell model calculation is coded as *CW5082* in OXBASH. The *CW5082* interaction originated from *KH5082* interaction [44] on replacing the proton $N = 4$ *two-body matrix elements* (TBME) with the effective interaction of Kruse and Wildenthal [45]. The KH5082 interaction utilizes the TBME of bare particle–particle and one particle–one hole (1p1h) "*bubble*" Kuo–Herling (KH) interaction [46–48].

Table 2
The restrictions imposed on different subshells (partitions) in the shell model calculation

| P/N | Orbitals | $^{142}$Nd | | $^{144}$Nd | | $^{146}$Nd | |
|-----|----------|------|------|------|------|------|------|
| | | Max. | Min. | Max. | Min. | Max. | Min. |
| Proton | $1g_{\frac{7}{2}}$ | 8 | 6 | 8 | 7 | 8 | 7 |
| | $2d_{\frac{5}{2}}$ | 4 | 0 | 2 | 0 | 2 | 0 |
| | $2d_{\frac{3}{2}}$ | 4 | 0 | 2 | 0 | 2 | 0 |
| | $3s_{\frac{1}{2}}$ | 2 | 0 | 2 | 0 | 2 | 0 |
| | $2h_{\frac{11}{2}}$ | 4 | 0 | 2 | 0 | 2 | 0 |
| Neutron | $1h_{\frac{9}{2}}$ | ... | ... | 2 | 0 | 4 | 0 |
| | $2f_{\frac{7}{2}}$ | ... | ... | 2 | 0 | 2 | 0 |
| | $2f_{\frac{5}{2}}$ | ... | ... | 2 | 0 | 4 | 0 |
| | $3p_{\frac{3}{2}}$ | ... | ... | 2 | 0 | 4 | 0 |
| | $3p_{\frac{1}{2}}$ | ... | ... | 2 | 0 | 2 | 0 |
| | $1i_{\frac{13}{2}}$ | ... | ... | 2 | 0 | 4 | 0 |

The *single particle energies* used in the calculation are taken from experiment ([44] and references therein). The values used are $\varepsilon(\pi g_{7/2}) = -9.5958$, $\varepsilon(\pi d_{5/2}) = -8.6755$, $\varepsilon(\pi d_{3/2}) = -6.9352$, $\varepsilon(\pi s_{1/2}) = -6.9278$, $\varepsilon(\pi h_{11/2}) = -6.8379$, $\varepsilon(\nu h_{9/2}) = -0.8950$, $\varepsilon(\nu f_{7/2}) = -2.38$, $\varepsilon(\nu f_{5/2}) = -0.89$, $\varepsilon(\nu p_{3/2}) = -1.625$, $\varepsilon(\nu p_{1/2}) = -1.16$, $\varepsilon(\nu i_{13/2}) = -0.29$ MeV. The resultant energy levels are shown in Fig. 3 along with the level scheme obtained from experiment.

The calculated *occupation numbers* of all the fully or partially occupied valence orbitals are given in Table 3. These numbers have been used with single particle radial wavefunctions generated by a bound state potential of the Woods–Saxon form plus a
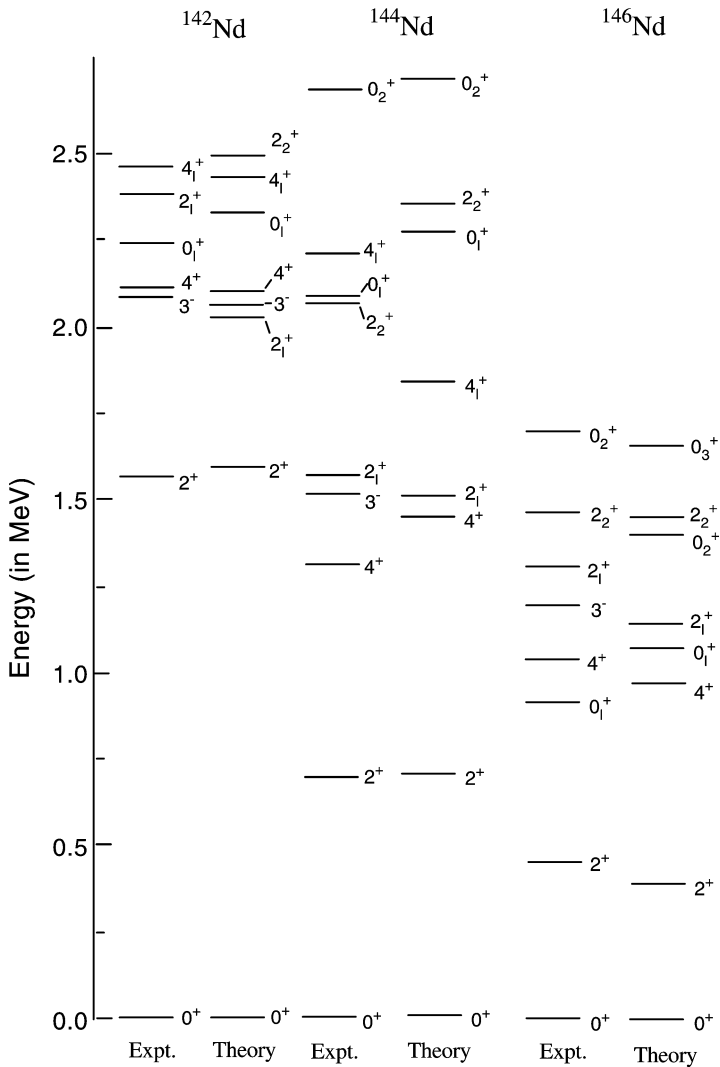


Fig. 3. The experimental and theoretically calculated (shell model) energy level diagram for $^{142,144,146}$Nd.

Table 3
Calculated occupation numbers in the ground states of neodymium nuclei

| P/N | Orbitals | Nucleus | | |
|---|---|---|---|---|
| | | $^{142}$Nd | $^{144}$Nd | $^{146}$Nd |
| Proton | $1g_{\frac{7}{2}}$ | 7.981 | 8.0 | 8.0 |
| | $2d_{\frac{5}{2}}$ | 1.732 | 1.793 | 2.0 |
| | $2d_{\frac{3}{2}}$ | 0.043 | 0.031 | 0.0 |
| | $3s_{\frac{1}{2}}$ | 0.037 | 0.019 | 0.0 |
| | $2h_{\frac{11}{2}}$ | 0.208 | 0.157 | 0.0 |
| Neutron | $1h_{\frac{9}{2}}$ | 0.0 | 0.192 | 1.002 |
| | $2f_{\frac{7}{2}}$ | 0.0 | 1.238 | 1.6 |
| | $2f_{\frac{5}{2}}$ | 0.0 | 0.15 | 0.848 |
| | $3p_{\frac{3}{2}}$ | 0.0 | 0.129 | 0.172 |
| | $3p_{\frac{1}{2}}$ | 0.0 | 0.044 | 0.379 |
| | $1i_{\frac{13}{2}}$ | 0.0 | 0.247 | 0.0 |

Table 4
Woods–Saxon potential parameters used to calculate the single particle wave functions

| N/P | $V_0$ MeV | $r_0$ fm | $a_0$ fm | $V_{so}$ MeV | $r_{so}$ fm | $a_{so}$ fm | $r_c$ fm |
|---|---|---|---|---|---|---|---|
| Proton | 59.312 | 1.268 | 0.802 | 6.0 | 1.10 | 0.65 | 1.218 |
| Neutron | 47.397 | 1.243 | 0.723 | 6.0 | 1.10 | 0.65 | |

standard spin–orbit potential to construct the ground state densities of the isotopes. The bound state potential parameters, shown in Table 4, are used in an orbit independent method. We have searched for appropriate single particle binding energies by keeping the parameters same for all the orbits. The *one body density matrices* (OBDM) ($D^i_{jj'}$, $i =$ p, n) derived from shell model wavefunctions and listed in Table 5, are used in the computer code DENS [49] with the same bound state potential to generate the $0^+ \rightarrow 2^+$ transition densities.

Tassie Model [50] is assumed to calculate the core polarization contribution. The coefficients obtained are suitably adjusted to reproduce the experimental electric transition rates. In the present study, effective charges of $e_p = 2.1e$ and $e_n = 1.1e$ are found to be necessary for all the three isotopes. The values of the effective charges are on the higher side possibly because of the truncation used for the configuration space. A comparison of estimated $B$(E2) values with the experimental data is shown in Table 6. A shell model calculation for the doubly magic $^{16}$O is also performed to obtain the required ground state density.

The calculated nuclear densities, ground state as well as $0^+ \rightarrow 2^+$ transition densities of $^{142,144,146}$Nd isotopes are shown in Figs. 4 and 5. The charge transition densities from inelastic electron scattering experiments [33,51,52] are shown in Figs. 5(a), (c), (d)

Table 5
One-body transition density matrix elements calculated for the $0^+$ to $2^+$ transitions

| $j-j'$ | $^{142}$Nd $D^p_{jj'}$ | $D^n_{jj'}$ | $j-j'$ | $^{144}$Nd $D^p_{jj'}$ | $D^n_{jj'}$ | $^{146}$Nd $D^p_{jj'}$ | $D^n_{jj'}$ |
|---|---|---|---|---|---|---|---|
| $\frac{7}{2}-\frac{7}{2}$ | $-0.00262$ | - | $\frac{5}{2}-\frac{5}{2}$ | $-0.74372$ | – | $0.69490$ | – |
| $\frac{7}{2}-\frac{5}{2}$ | $-0.05103$ | - | $\frac{5}{2}-\frac{3}{2}$ | $0.00008$ | – | – | – |
| $\frac{7}{2}-\frac{3}{2}$ | $0.00074$ | - | $\frac{5}{2}-\frac{1}{2}$ | $-0.00025$ | – | – | – |
| $\frac{5}{2}-\frac{7}{2}$ | $0.00461$ | – | $\frac{3}{2}-\frac{5}{2}$ | $-0.00057$ | – | – | – |
| $\frac{5}{2}-\frac{5}{2}$ | $0.00812$ | – | $\frac{3}{2}-\frac{3}{2}$ | $0.00085$ | – | – | – |
| $\frac{5}{2}-\frac{3}{2}$ | $0.07128$ | – | $\frac{3}{2}-\frac{1}{2}$ | $0.00013$ | – | – | – |
| $\frac{5}{2}-\frac{1}{2}$ | $0.46005$ | – | $\frac{1}{2}-\frac{5}{2}$ | $-0.00171$ | – | – | – |
| $\frac{3}{2}-\frac{7}{2}$ | $-0.04333$ | – | $\frac{1}{2}-\frac{3}{2}$ | $-0.00011$ | – | – | – |
| $\frac{3}{2}-\frac{5}{2}$ | $0.00872$ | – | $\frac{11}{2}-\frac{11}{2}$ | $-0.00284$ | – | – | – |
| $\frac{3}{2}-\frac{3}{2}$ | $-0.01636$ | – | $\frac{9}{2}-\frac{9}{2}$ | – | $-0.01117$ | – | $0.20812$ |
| $\frac{3}{2}-\frac{1}{2}$ | $0.36517$ | – | $\frac{7}{2}-\frac{7}{2}$ | – | $-0.21163$ | – | $0.38532$ |
| $\frac{1}{2}-\frac{5}{2}$ | $0.00719$ | – | $\frac{5}{2}-\frac{5}{2}$ | – | $-0.00991$ | – | $0.17206$ |
| $\frac{1}{2}-\frac{3}{2}$ | $0.04136$ | – | $\frac{3}{2}-\frac{3}{2}$ | – | $-0.01378$ | – | $0.01648$ |
| $\frac{11}{2}-\frac{11}{2}$ | $-0.00262$ | – | $\frac{13}{2}-\frac{13}{2}$ | – | $-0.01875$ | – | – |

Table 6
Experimental and calculated (shell model) transition rates for neodymium isotopes

| Nuclei | $N$ | $Z$ | $B$(E2) $(e^2\,\text{fm}^4)$ Expt. | Calc. | $M_p$ $(e\,\text{fm}^2)$ Calc. | $M_n$ $(e\,\text{fm}^2)$ |
|---|---|---|---|---|---|---|
| $^{142}$Nd | 82 | 60 | 2810[a] | 2908 | $-53.93$ | $-35.95$ |
| $^{144}$Nd | 84 | 60 | 4600[b] | 3683 | $-60.69$ | $-53.74$ |
| $^{146}$Nd | 86 | 60 | 6910[c] | 7745 | $-88.01$ | $-97.47$ |

[a] Ref. [52];
[b] Ref. [51];
[c] Ref. [33].

with open circles. The calculated point proton distributions reproduce the shape of the experimental data quite well at large radius but underestimate the magnitudes slightly. It is to be noted that $^{142}$Nd being a spherical nucleus with $N = 82$ closed neutron shell, the excitations, especially the low-lying excitations will mostly involve the proton configurations. With 2 and 4 valence neutrons, respectively, the excitations in $^{144}$Nd and $^{146}$Nd, on the other hand, will receive increasing contributions from neutron configurations. The feature is distinctly evident in Fig. 5(b) where the behaviours of neutron transition densities for $0^+ \rightarrow 2^+_1$ excitations in $^{142,144,146}$Nd have been compared at large radial values. The prominent surface peaked distributions of the transition densities in these isotopes indicate the dominant collective nature of the first $2^+$ excitations. In an attempt to estimate the accuracy of our shell model calculations, we plotted, in Fig. 6, the quantity
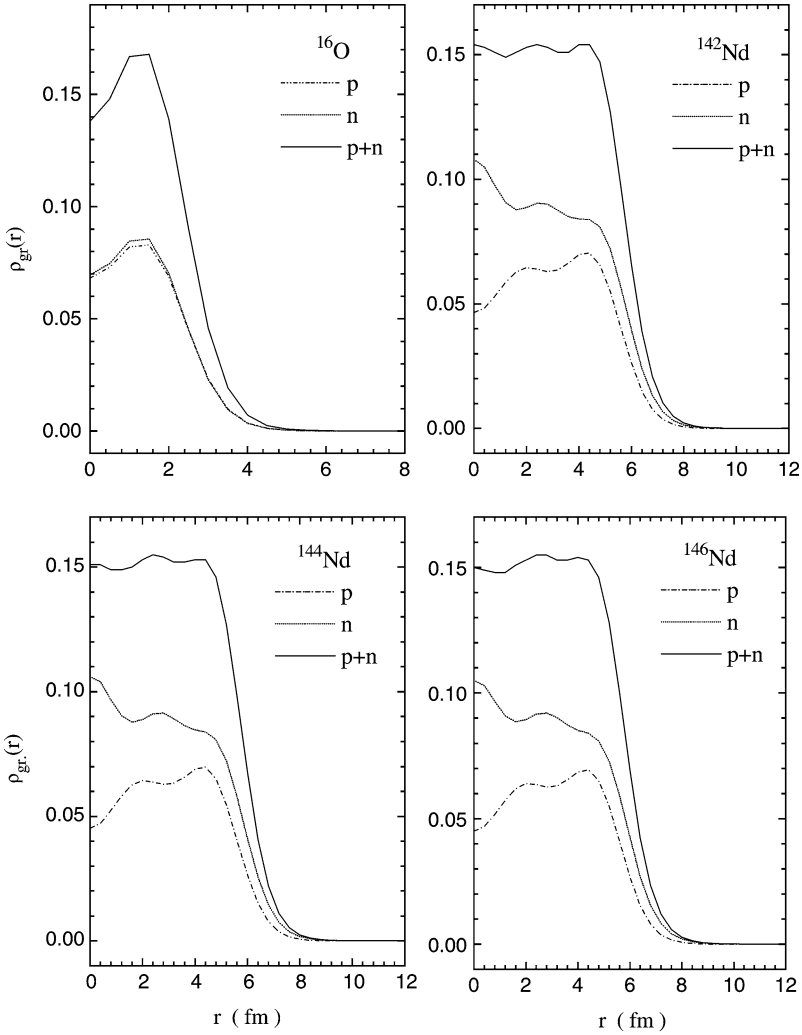
Fig. 4. The ground state density distributions of $^{16}$O and $^{142,144,146}$Nd using shell model wave function. Here p and n represent the proton and neutron distributions, respectively.

$\Re$, the ratio of transition matrix elements $\widetilde{M}_{pp}$ and $\widetilde{M}_{dd}$ derived from $(p, p')$ and $(d, d')$ scattering [53], as a function of mass number $A$. This ratio in turn depends upon the neutron and proton transition matrices $M_n$ and $M_p$. The calculated $\Re$ using the shell model $M_n$ and $M_p$ values for each mass lies within the range of experimental errors. However, the experimental points (bullets) and quasiparticle phonon model (QPM) calculations (box) denote the mean value of the ratio over the ensemble of transition matrix elements determined for a given mass. We calculated $\Re$ only with matrix elements for quadrupole excitation of $0^+ \rightarrow 2^+$.
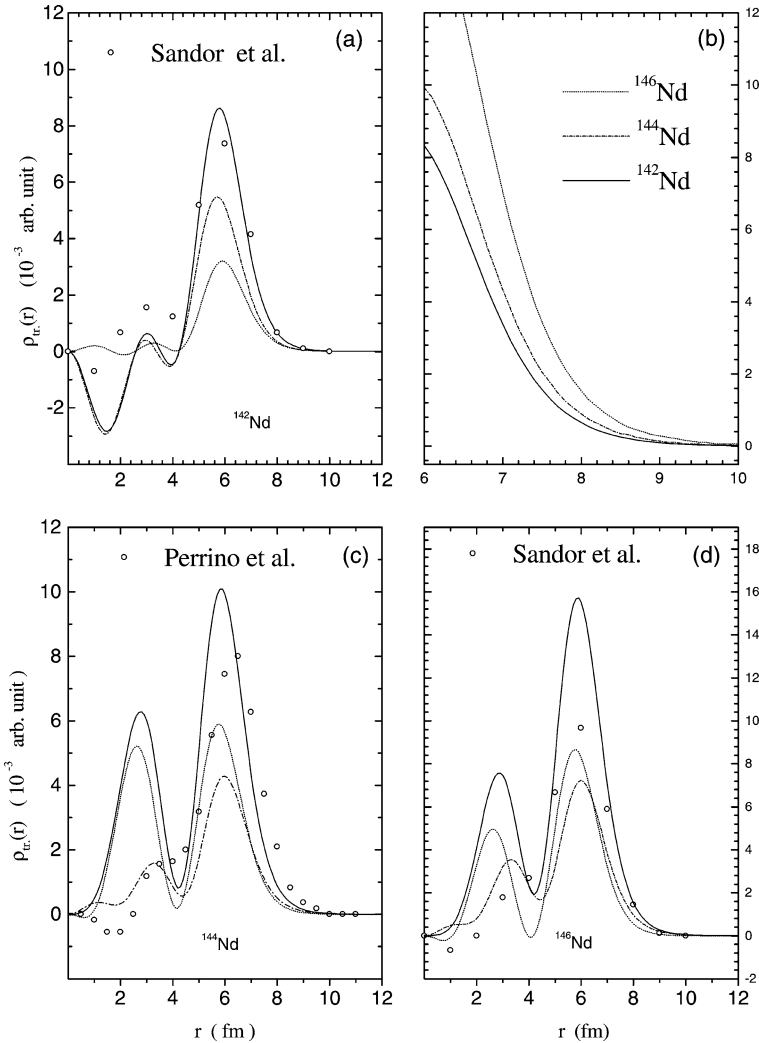
Fig. 5. The transition density distributions of $^{142,144,146}$Nd using shell model wave function along with the electron scattering data taken from Refs. [33,52,53]. Here dotted and dashed-dotted lines represent the neutron and proton distributions, respectively.

## 3.2. The imaginary Feshbach potential

In the model proposed by Vinh Mau [27] based on Feshbach formalism [14], the generalized optical potential for elastic scattering at energy $E$ can be written as

$$
\begin{aligned}
V_{\text{opt}}(E, r, r') &= \langle \Phi_0 | V | \Phi_0 \rangle + \langle \Phi_0 | V Q \frac{1}{E - H_{QQ} + i\epsilon} Q V | \Phi_0 \rangle \\
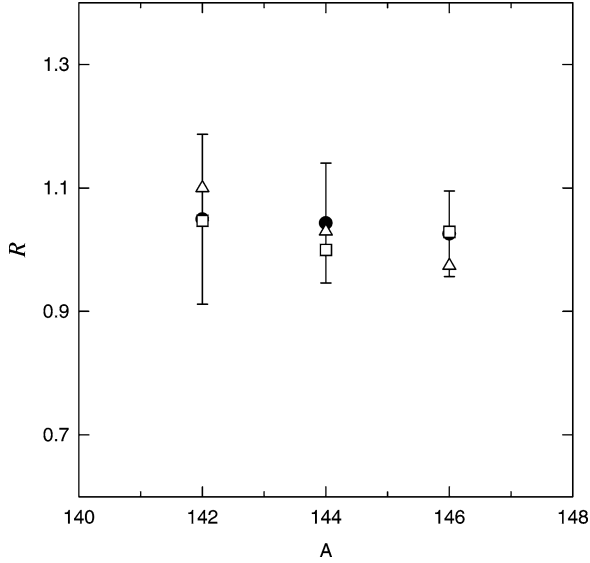&= V_0 + \Delta V,
\end{aligned}
\tag{10}
$$

Fig. 6. Ratios ($\Re$) of quadrupole transition matrix elements from (p, p′) and (d, d′) experiments (black dot) with QPM (box) and shell model (triangle) predictions.

where $\Phi_0$ is the ground state wavefunction, $Q$ is the projection operator that projects off the open channels, $H$ is the total Hamiltonian and $V$ is the interaction operator. The generalised potential, thus, can be expressed as a sum of $V_0$, the double folded potential and $\Delta V$, the polarization potential coming from the coupling of non-elastic channels (included in the $Q$-projection of the channel space) to the open channel (here the elastic channel). The term $\Delta V$ is complex, non-local and energy dependent in nature with the imaginary $\Delta V$ contributing the absorptive potential required in the optical model analysis.

In the weak coupling limit, one can write the polarization potential for inelastic excitations as [16]

$$\Delta V^{\text{in}}(\mathbf{r}, \mathbf{r}') = \sum_{\alpha \neq 0} V_\alpha^*(\mathbf{r}) G_\alpha(\mathbf{r}, \mathbf{r}') V_\alpha(\mathbf{r}'),  \tag{11}$$

where $\alpha$ denotes the possible inelastic excitation channels. The $G_\alpha(\mathbf{r}, \mathbf{r}')$ is the Green's function for propagation of the system in channel $\alpha$ and can be approximated by the WKB propagator [27]. $V_\alpha$, denoting the transition matrix element for a state $\alpha$ of angular momentum $\lambda$ and projection $\mu$, can be written as shown in Ref. [16],

$$V_\alpha(\mathbf{r}) = \frac{1}{\sqrt{2\lambda + 1}} f_\lambda^{(\alpha)}(r) Y_\lambda^\mu(\mathbf{r})  \tag{12}$$

where $f_\lambda^{(\alpha)}(r)$ represents the nuclear form factor for the state $\alpha$ of angular momentum $\lambda$. In our analysis the form factor has been determined from Copenhagen potential [54] assuming vibrational excitations and taking the derivative of the potential as the formfactor. The strengths of the target excitation channels are taken from [53] while those for the projectile

excitations are from [17]. The local equivalent of $\mathrm{Im}\,\Delta V^{\mathrm{in}}(\mathbf{r}, \mathbf{r}')$ in the case of weak non-locality can be written as

$$\mathrm{Im}\,\Delta V^{\mathrm{in}}(R) \equiv W_{\mathrm{fes}}(R) = \frac{mM}{2\pi k\hbar^2} \sum_{\lambda, \alpha \neq 0} \left(\beta_{\lambda i}^{(\alpha)}\right)^2 I_\alpha(R), \tag{13}$$

where $\beta_{\lambda i}^{(\alpha)}$ denotes the strength of excitation of nucleus $i$ (target or projectile) with multipolarity $\lambda$ in channel $\alpha$. The integration $I_\alpha(R)$ corresponding to channel $\alpha$ is given by

$$I_\alpha(R) = \int_0^{2R} ds\, e^{(-\kappa_\alpha s)} \sin(ks) \sin(k_\alpha s) \left[ \left.\frac{\partial U^c(r)}{\partial r}\right|_{r=R+s/2} \left.\frac{\partial U^c(r)}{\partial r}\right|_{r=R-s/2} \right] \tag{14}$$

in terms of the coordinates $\mathbf{R} = \frac{1}{2}(\mathbf{r} + \mathbf{r}')$ and $\mathbf{s} = \mathbf{r} - \mathbf{r}'$ with

$$k_\alpha^2 = \frac{mM}{\hbar^2}\left[ E_{\mathrm{cm}} - E_\alpha^* + \sqrt{(E_{\mathrm{cm}} - E_\alpha^*)^2 + W_{\mathrm{fes}}^2(R)} \right],$$

$$\kappa_\alpha = \frac{mM}{\hbar^2}\frac{W_{\mathrm{fes}}(R)}{k_\alpha}, \tag{15}$$

$$E_\alpha^* = E_\alpha + V_0(R) + \Delta V(R) + V_{\mathrm{C}}(R). \tag{16}$$

The local momentum $k(R)$ is given by Eq. (4) and $m$ is the reduced mass and $M$ is the nucleon mass in MeV. We derived the $\Delta V$ polarization potential for $^{16}\mathrm{O} + {}^{142,144,146}\mathrm{Nd}$ systems at necessary energies following the prescription of Pacheco et al. [16]. The derivation included the dominant target inelastic excitations up to 3 MeV energy below which the excitations are primarily one-step in nature and the $3^-$ (6.13 MeV), $2^+$ (6.92 MeV) and $2^+$ (11.52 MeV) states of projectile $^{16}\mathrm{O}$. The potential contributions of these channels are evaluated term by term. The calculated imaginary Feshbach potentials $W_{\mathrm{fes}}(R)$ for $^{16}\mathrm{O} + {}^{142,144}\mathrm{Nd}$ have been shown with dotted lines in Fig. 10.

### 3.3. Coupled channel calculation with Feshbach potential

In the evaluation of complex polarization potential $\Delta V$ at each energy, described in the previous section, only the open channels contribute to produce the imaginary part. On the other hand, all the open and closed channels contribute to form the real polarization potential. Since, we included only the dominant open inelastic channels to produce the necessary absorption of flux from the elastic channel, the effect of polarization of real potential was incorporated through a renormalization factor and the effective real potential was, therefore, of the form

$$V_0 + \Delta V_{\mathrm{R}} = \lambda_{\mathrm{R}}(E) V_{\mathrm{folded}}. \tag{17}$$

In the coupled channel (CC) calculation, performed with the code ECIS94 [55], we have considered explicit coupling to first $2^+$ state of Nd target. In the first step, we analysed the data with the renormalizable folded real potential and the two component imaginary potential of Eq. (2). The imaginary renormalization factor $\lambda_{\mathrm{I}}$ for $W_{\mathrm{fes}}$ was set equal to

unity. The folded transition potential for $0^+ \rightarrow 2^+_1$ transition was used as the real nuclear coupling formfactor. As there is no standard prescription available for imaginary coupling potential, we assumed the imaginary formfactor to be of the same shape as the real one but its strength was reduced by 50% [56]. The normalization constants of unity and 0.5 for real and imaginary coupling potentials respectively were kept constant throughout the CC calculation. Thus in the CC analyses with $W_F + W_{fes}$ the only variable parameter was the real renormalization factor $\lambda_R$. We varied the factor $\lambda_R(E)$ to obtain simultaneously good fit to the elastic and inelastic angular distributions. The resulting fits to the data are shown in Figs. 7, 8, 9 with dashed lines. Reasonably good fits to the angular distributions at all the energies are obtained for $^{16}O + ^{146}Nd$ but for $^{16}O + ^{142,144}Nd$ systems the calculated angular distributions show steeper fall off at large angles compared to the data. From Figs. 7 and 8 it is to be noted that the calculated angular distributions for both elastic
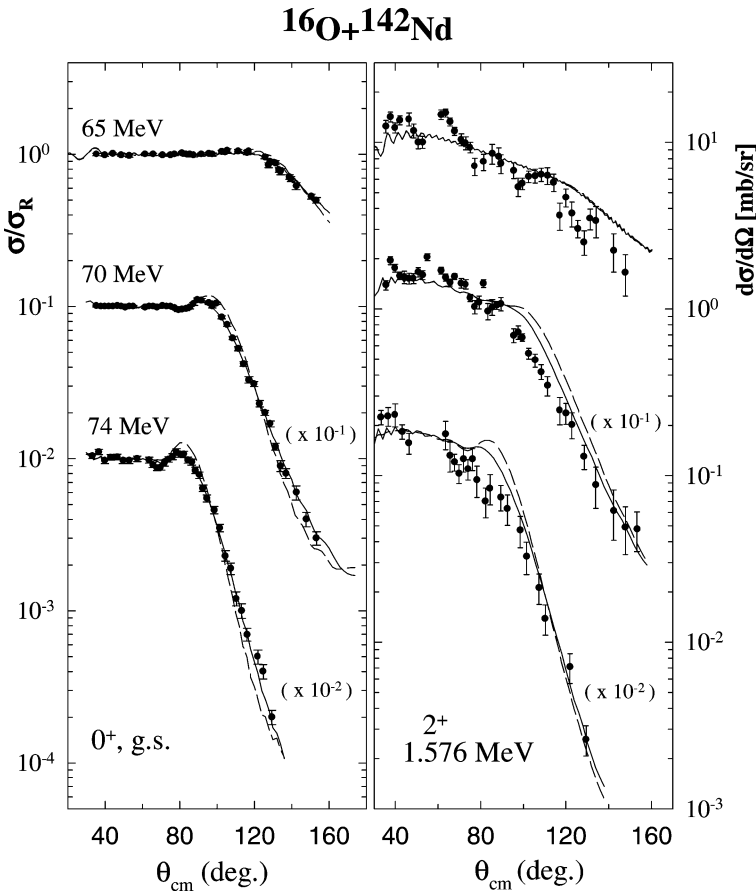


Fig. 7. Coupled channel calculations (solid curves) for elastic and inelastic angular distributions of $^{16}O + ^{142}Nd$ system. The dashed curves represent the angular distributions obtained from coupled channel calculation without the surface imaginary term ($W_S$).
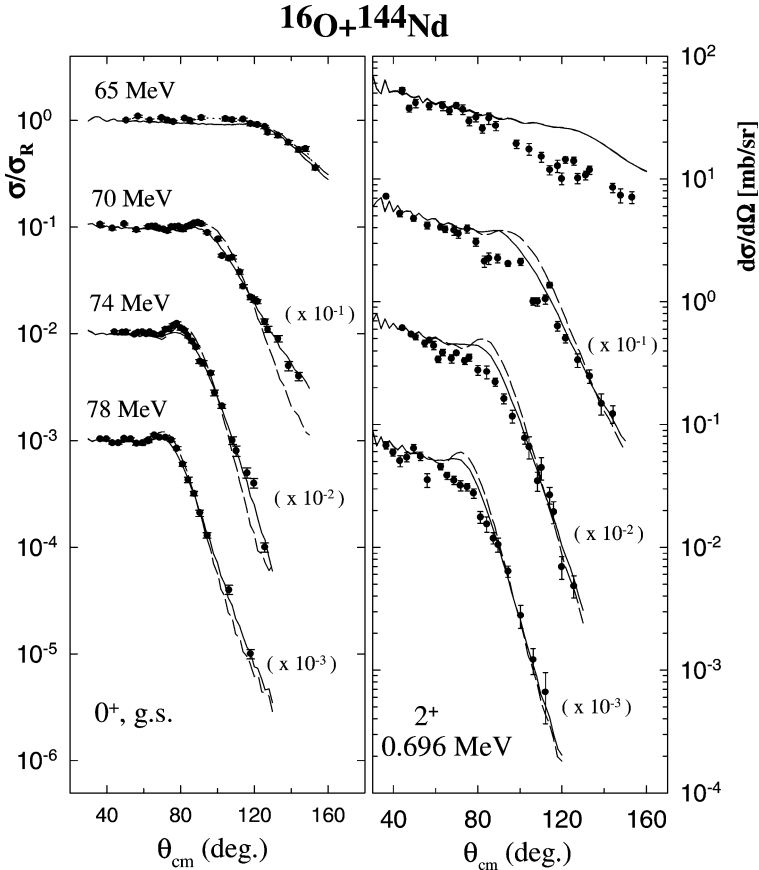
$$^{16}O+^{144}Nd$$



Fig. 8. Same as Fig. 7 but for $^{16}O + ^{144}Nd$.

and inelastic scattering over predict the data around $\Theta_{cm} = 80°$. On the top of the barrier at 65 MeV, the imaginary potential $W_F + W_{fes}$ reproduces the elastic data quite well but not the inelastic angular distributions. For the relatively deformed $^{146}Nd$ target, on the other hand, the microscopically calculated imaginary potential due to inelastic excitations, along with $W_F$, seems to be sufficient to generate the overall absorption at all the energies. The best fit values of the real renormalizations for all the cases are shown in Table 7.

To investigate further this lack of absorption, we introduced a phenomenological surface Woods–Saxon potential to enhance the absorption in the large radial region as was done by Pacheco et al. [17]. The total imaginary potential now consists of three terms

$$W(\mathbf{R}, E) = W_F(\mathbf{R}) + W_{fes}(\mathbf{R}, E) + W_s(\mathbf{R}, E). \tag{18}$$

All the data were refitted with this new imaginary potential. Same optical potential was used for both the channels considered in the coupling scheme. In this step, we fitted first the 78 MeV data for $^{16}O + ^{144,146}Nd$ and 74 MeV data for $^{16}O + ^{142}Nd$ systems. All the four parameters, i.e., $\lambda_R$ and $(W_s^0, R_s, a_s)$ were varied simultaneously to obtain the best fits.
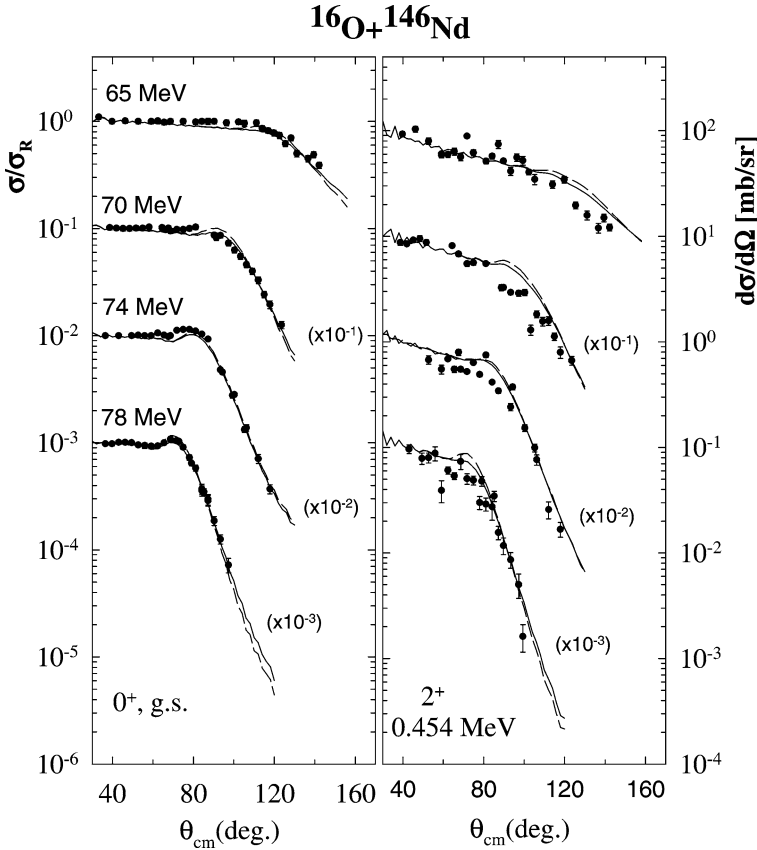
$^{16}$O+$^{146}$Nd



Fig. 9. Same as Fig. 7 but for $^{16}$O + $^{146}$Nd.

The resulting parameters are also given in Table 7. Subsequently to reproduce the lower energy data we kept the radius parameter of the surface potential fixed to that obtained from the search over the highest energy data. Therefore, only two parameters were varied in the search procedure to fit the lower energy data. The fits to the data at all the incident energies for both $^{16}$O + $^{142,144}$Nd systems improved significantly except for the inelastic angular distributions at 65 MeV. The effect of introducing the additional surface absorption was found to be minimum for more deformed $^{16}$O + $^{146}$Nd system.

In Fig. 10, the imaginary potentials resulted from the simultaneous fits to the elastic and inelastic data for $^{16}$O + $^{142,144}$Nd have been shown. It is clear from the figure that the empirical surface absorption term has a longer range compared to the Feshbach absorptive potential and peaks on or beyond the tail of $W_{fes}(R)$. It is difficult to ascertain exactly the type of reaction channels contributing to this additional term. $W_{fes}$ was constructed with contributions from target excitations upto 3 MeV having significant transition probabilities. Altogether 9 excited states of $^{142}$Nd and 13 excited states each of $^{144}$Nd and $^{146}$Nd were considered to calculate the Feshbach potentials. Contributions from states with still higher excitation energies may have some non-negligible effect. For instance, in $^{142}$Nd there are

Table 7
Best fit parameters obtained from coupled channels calculations with $0^+$–$2^+$ coupling ($r_c = 1.25$ fm)

| System | $E_{\text{Lab}}$ | $\lambda_R$ | $\lambda_I$ | $W_s^0$ | $R_s$ | $a_s$ | $Q_{22}$ ($e$b) |
|---|---|---|---|---|---|---|---|
| $^{16}$O + $^{142}$Nd | 65 | 1.42 | 1.0 | | | | |
| | | 1.32 | 1.0 | 2.70 | 10.508 | 0.257 | −0.20 |
| | 70 | 1.26 | 1.0 | | | | ... |
| | | 1.18 | 1.0 | 4.02 | 10.508 | 0.335 | ... |
| | 74 | 1.35 | 1.0 | | | | ... |
| | | 1.05 | 1.0 | 2.14 | 10.508 | 0.462 | ... |
| $^{16}$O + $^{144}$Nd | 65 | 1.26 | 1.0 | | | | |
| | | 1.19 | 1.0 | 1.68 | 10.541 | 0.492 | −0.39 |
| | 70 | 1.15 | 1.0 | | | | ... |
| | | 1.18 | 1.0 | 7.03 | 10.541 | 0.304 | ... |
| | 74 | 1.14 | 1.0 | | | | ... |
| | | 1.02 | 1.0 | 3.05 | 10.541 | 0.402 | ... |
| | 78 | 1.20 | 1.0 | | | | ... |
| | | 1.06 | 1.0 | 2.71 | 10.541 | 0.426 | ... |
| $^{16}$O + $^{146}$Nd | 65 | 1.36 | 1.0 | | | | |
| | | 1.19 | 1.0 | 0.75 | 10.568 | 0.492 | −0.72 |
| | 70 | 1.18 | 1.0 | | | | ... |
| | | 1.07 | 1.0 | 0.19 | 10.568 | 0.919 | ... |
| | 74 | 1.05 | 1.0 | | | | ... |
| | | 1.04 | 1.0 | 0.11 | 10.568 | 0.919 | ... |
| | 78 | 1.17 | 1.0 | | | | ... |
| | | 1.02 | 1.0 | 0.34 | 10.568 | 0.919 | ... |

Note: The imaginary potential in all the cases includes a squared vol. WS potential $W_F$: $W_F^0 = 60.0$ MeV, $r_F = 1.0$ fm and $a_F = 0.4$ fm.

at least six states within 3 to 4 MeV excitation which have reduced isoscalar transition probabilities in the range of 2 to 9 Weisskopf units and these states have non-negligible contributions. But, the collective contribution of these omitted states peaks near 9.5 fm and falls off to insignificant values near 11 fm. The excitations of projectile $^{16}$O besides those considered do not contribute at those large radius values. Thus the empirical surface imaginary potential $W_S$ which peaks at larger radius ($\sim 11$ fm) originates predominantly from channels other than the omitted target excited states. We assume that this long range surface absorptive potential, necessary to fit the $^{142}$Nd and $^{144}$Nd angular distributions, simulates the absorption in transfer channels. Also the effect of this transfer absorption is more prominent close to the barrier energy and decreases as the incident energy increases.

It is to be noted that the observed lack of absorption is quite prominent in the inelastic channel as well for all the incident energies except near the top of the barrier ($\sim 65$ MeV). The improvement in the optical potential with the additional surface absorptive potential also improved the fits to the measured inelastic angular distributions. We included the *reorientation coupling* term in the coupled channel calculation in an attempt to improve further the fit to the inelastic data. The quadrupole moment values used [57] are shown in Table 7. But the inclusion of reorientation coupling term did not produce any significant change on the inelastic angular distributions. However, it is obvious from the fits that the
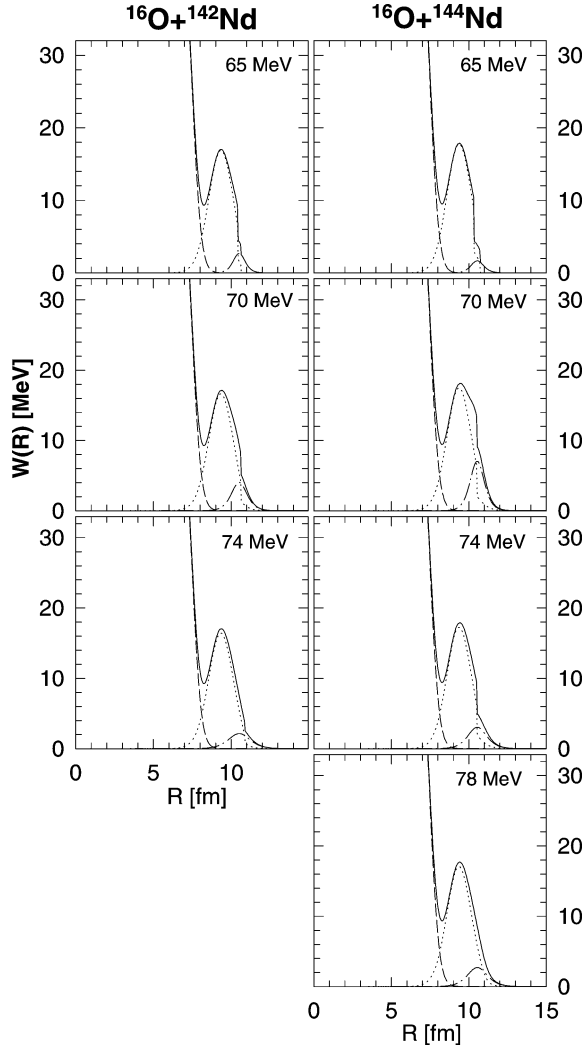
Fig. 10. Imaginary potentials used in the CC calculation for $^{16}$O + $^{142,144}$Nd. The dashed line represents $W_F$, the interior fusion potential. $W_{fes}$, the Feshbach potential, and the empirical surface absorptive potential $W_S$ are represented by dotted and dashed-dotted curves, respectively.

microscopic $0^+ \rightarrow 2^+$ nuclear form factor derived from the shell model wavefunctions provide reasonably good description of inelastic scattering data.

## 4. Summary

The angular distributions of elastic and inelastic scattering to $2_1^+$ for $^{16}$O + $^{142,144,146}$Nd systems have been measured in the vicinity of the Coulomb barrier (65 to 78 MeV)

and analysed in a systematic way using a coupled channel formalism with the necessary potentials derived from a microscopic consideration. Attempts have been made to simultaneously reproduce the elastic and inelastic angular distributions.

The microscopic approach to the analyses is based on two aspects. Firstly, we performed a truncated shell model calculation to obtain the ground state and $0^+ \rightarrow 2_1^+$ transition densities. The shell model calculations with the chosen basis is quite successful in reproducing the experimental level schemes of neutron shell closed $^{142}$Nd isotope as well as $^{144}$Nd and $^{146}$Nd nuclei with two and four valence nucleons respectively. The resulting transition densities and transition matrix values describe the experimental data reasonably well (Figs. 5 and 6). The derived densities are subsequently used to fold the density and energy dependent effective M3Y interaction. With the renormalization factors these folded diagonal and off-diagonal potentials are used in the coupled channel consideration. The fits to the inelastic scattering data justify the use of microscopic form factors obtained from shell model calculations.

Secondly, the contribution of coupling to inelastic excitations, except the $2_1^+$ excitation, has been evaluated term by term within the Feshbach formalism considering the excitations upto 3 MeV energy for all the isotopes. This microscopic energy dependent imaginary component along with an interior potential simulating the absorption due to fusion reproduced the data of relatively deformed $^{16}$O + $^{146}$Nd quite well. On the other hand, for $^{16}$O + $^{142,144}$Nd systems the potential ($W_F + W_{fes}$) is found to be inadequate in generating the necessary absorption. The observed lack of absorption is also quite distinct in the inelastic channel. Significant improvements have been observed in the fits to the measured angular distributions of $^{16}$O + $^{142,144}$Nd with an additional long ranged surface absorption. While for $^{16}$O + $^{146}$Nd the additional surface absorption does not affect the nature of the fits very much. The observation indicates that the Feshbach imaginary potential is sufficient to produce the required surface absorption in case of $^{146}$Nd target. Same inference has been derived by Pacheco et al. [17] in their analyses of elastic scattering from deformed targets. The added surface absorption term has a longer range compared to the Feshbach potential for inelastic excitation. It has been found that omitted higher inelastic excitations cannot introduce this absorption at large radius. A detailed coupled reaction channel claculation is in progress to identify the origin of this long range absorption which is more prominent just above the barrier energy.

## Acknowledgements

# References

[1] R.A. Broglia, G. Pollarolo, A. Winther, Nucl. Phys. A 361 (1981) 307.
[2] I.J. Thompson, M.A. Nagarajan, J.S. Lilley, B.R. Fulton, Phys. Lett. B 157 (1985) 250.
[3] S.C. Pieper, M.J. Rhoades-Brown, S. Landowne, Phys. Lett. B 162 (1985) 43.
[4] H. Esbensen, S. Landowne, Nucl. Phys. A 492 (1989) 473.
[5] C.H. Dasso, S. Landowne, G. Pollarolo, A. Winther, Nucl. Phys. A 459 (1989) 99.
[6] M. Beckerman, Phys. Rep. 129 (1985) 145.
[7] V. Baeza, B. Bilwes, R. Bilwes, J. Diaz, J.L. Ferrero, Nucl. Phys. A 419 (1984) 412.
[8] J.S. Lilley, B.R. Fulton, M.A. Nagarajan, I.J. Thompson, D.W. Barnes, Phys. Lett. B 151 (1985) 181.
[9] B.R. Fulton, D.W. Barnes, J.S. Lilley, M.A. Nagarajan, I.J. Thompson, Phys. Lett. B 162 (1985) 55.
[10] B. Bilwes, R. Bilwes, J. Diaz, J.L. Ferrero, Nucl. Phys. A 449 (1986) 519.
[11] M.A. Nagarajan, C. Mahaux, G.R. Satchler, Phys. Rev. Lett. 54 (1984) 1136.
[12] C. Mahaux, H. Ngô, G.R. Satchler, Nucl. Phys. A 449 (1986) 354.
[13] G.R. Satchler, Phys. Rep. 199 (1991) 147.
[14] H. Feshbach, Ann. Phys. 5 (1958) 357;
     H. Feshbach, Ann. Phys. 19 (1962) 287.
[15] J.M. Barrigon, A. Baeza, J.L. Ferrero, J.C. Pacheco, B. Bilwes, R. Bilwes, Nucl. Phys. A 545 (1992) 720.
[16] J.C. Pacheco, B. Bilwes, F. Sánchez, J.A. Ruiz, J. Diaz, J.L. Ferrero, D. Kadi-Hanifi, Nucl. Phys. A 588 (1995) 537.
[17] J.C. Pacheco, M.D. Kadi-Hanifi, B. Bilwes, F. Ramiro, Phys. Rev. C 59 (1999) 314.
[18] N. Keeley, J.A. Christley, N.M. Clarke, B.R. Fulton, J.S. Lilley, M.A. Nagarajan, I.J. Thompson, Nucl. Phys. A 582 (1995) 314.
[19] N. Keeley, J.S. Lilley, J.A. Christley, Nucl. Phys. A 603 (1996) 97.
[20] D.T. Khoa, W. Von Oertzen, H.G. Bohlen, Phys. Rev. C 49 (1994) 1652.
[21] D.T. Khoa, O.M. Knyazkov, Z. Phys. A 328 (1987) 67.
[22] G.R. Satchler, W.G. Love, Phys. Rep. 55 (1979) 183.
[23] G.R. Satchler, Nucl. Phys. A 329 (1979) 233.
[24] G. Pollarolo, R.A. Broglia, A. Winther, Nucl. Phys. A 406 (1983) 369.
[25] D.M. Brink, Fl. Stancu, Phys. Rev. C 30 (1984) 1904.
[26] J.P. Jeukenne, A. Lejeune, C. Mahaux, Phys. Rev. C 16 (1977) 80.
[27] N. Vinh Mau, Nucl. Phys. A 457 (1986) 413;
     N. Vinh Mau, Nucl. Phys. A 470 (1987) 406;
     N. Vinh Mau, Inst. Phys. Conf. Ser. 110 (1990) 1.
[28] N. Vinh Mau, J.L. Ferrero, J.C. Pacheco, B. Bilwes, Nucl. Phys. A 531 (1991) 435.
[29] N. Vinh Mau, J.L. Ferrero, J.C. Pacheco, B. Bilwes, Phys. Rev. C 47 (1993) 899.
[30] N. Vinh Mau, J.C. Pacheco, J.L. Ferrero, B. Bilwes, Nucl. Phys. A 560 (1993) 879.
[31] J.L. Ferrero, J.C. Pacheco, A. Baeza, J.M. Barrigon, B. Bilwes, R. Bilwes, N. Vinh Mau, Nucl. Phys. A 514 (1990) 367.
[32] R. Bilwes, B. Bilwes, N. Vinh Mau, J.C. Pacheco, Nulc. Phys. A 526 (1991) 292.
[33] R.K.J. Sandor, H.P. Blok, M. Girod, M.N. Harakeh, C.W. de Jager, V.Yu. Ponomarev, H. de Vries, Nucl. Phys. A 551 (1993) 349.
[34] O. Scholten, H. Kruse, Phys. Lett. B 125 (1983) 113;
     O. Scholten, H.C. Wui, A.E.L. Dieperink, Z. Phys. A 332 (1989) 1.
[35] H. Sagawa, O. Scholten, B.A. Brown, B.H. Wildenthal, Nucl. Phys. A 462 (1987) 1.
[36] B.H. Wildenthal, in: A. Covello (Ed.), Proc. of 3rd Int. Spring Seminar on Nuclear Physics, Ischia, Italy 1990, World Scientific, Singapore, 1991, p. 35.
[37] A. Holt, T. Engeland, E. Osnes, M. Hjorth-Jensen, J. Suhonen, Nucl. Phys. A 618 (1997) 107.
[38] S. Mandal, D. Kabiraj, D.K. Avasthi, Nucl. Instrum. Methods A 397 (1997) 59.
[39] D.K. Avasthi, A. Tripathi, D. Kabiraj, S. Venkatramanan and S.K. Datta, Internal report of NSC, NSC/TR/DKA/92/16.
[40] G. Bertsch, J. Borysowicz, H. McManus, W.G. Love, Nucl. Phys. A 284 (1977) 399.
[41] D.T. Khoa, W. Von Oertzen, Phys. Lett. B 304 (1993) 8.
[42] B.A. Brown, A. Etchegoyen and W.D.M. Rae, The computer code OXBASH, MSU-NSCL report no. 524.

[43] S.S. Ghugre, Ph.D. Thesis, Bombay University, unpublished.
[44] W.T. Chou, E.K. Warburton, Phys. Rev. C 45 (1992) 1720.
[45] H.G. Kruse, B.H. Wildenthal, Bull. Am. Phys. Soc. 27 (1982) 533.
[46] T.T.S. Kuo and G. Herling, US Naval Research Laboratory Report, No 2258 (1971), unpublished.
[47] J.B. Mc Grory, Phys. Rev. C 8 (1973) 693.
[48] E.K. Warburton, B.A. Brown, Phys. Rev. C 43 (1991) 602.
[49] B.A. Brown, DENS computer programme, private communication.
[50] L.J. Tassie, Austr. J. Phys. 9 (1956) 407.
[51] R. Perrino, N. Blasi, R. de Leo, M.N. Harakeh, C.W. de Jager, S. Micheletti, J. Mierement, M. Pignanelli, V.Yu. Ponomarev, R.K.J. Sandor, H. de Vries, Nucl. Phys. A 561 (1993) 343.
[52] R.K.J. Sandor, H.P. Blok, U. Garg, M.N. Harakeh, C.W. de Jaeger, V.Yu. Ponomarev, A.I. Vdovin, H. de Vries, Nucl. Phys. A 535 (1991) 669.
[53] M. Pignanelli, N. Blasi, J.A. Bordewijk, R. de Leo, M.N. Harakeh, M.A. Hofstee, S. Micheletti, R. Perrion, V.Yu. Ponomarer, V.G. Soloviev, A.V. Sushkov, S.Y. van der Werf, Nucl. Phys. A 559 (1993) 1.
[54] R.A. Broglia, A. Winther, in: Heavy Ion Reactions, Vol. I, Addison-Wesley, 1991, p. 116.
[55] J. Raynal, Computer programme ECIS94, unpublished.
[56] G.R. Satchler, Direct Nuclear Reactions, Oxford Univ. Press, Oxford, 1983.
[57] D.L. Hillis, E.E. Gross, D.C. Hensley, C.R. Bingham, F.T. Baker, A. Scott, Phys. Rev. C 16 (1977) 1467.